https://doi.org/10.5194/se-2020-122
Preprint. Discussion started: 31 July 2020

Solid Earth Discussions

Imaging Seismic Wave-Fields with AlpArray and Neighboring European Networks

Marcel Tesch[1], Johannes Stampa[1], Thomas Meier[1], Edi Kissling[2], György Hetényi[3], Wolfgang Friederich[4], Michael Weber[5 6], Benjamin Heit[5], and the AlpArray Working Group[7]

[1] *Christian-Albrechts-Universität zu Kiel*

[2] *Eidgenössische Technische Hochschule Zürich*

[3] *Université de Lausanne*

[4] *Ruhr-Universität Bochum*

[5] *Deutsches GeoForschungsZentrum Potsdam*

[6] *Universität Potsdam*

[7] http://alparray.ethz.ch/

Abstract

The modern-day coverage and availability of broad-band stations in the greater Alpine area offered by AlpArray, Swath-D and the European seismological networks allows for imaging seismic wave-fields at yet unprecedented resolution. In the AlpArray area and in Italy, the distance of any point to the nearest station is less than $30km$, resulting in an average inter-station distance of about $45km$. With a much denser deployment in a smaller region of the Alps ($320km$ in length and $140km$ wide), the Swath-D network possesses an average inter-station distance of about $15km$.

We provide single event seismogram sections, time slices of teleseismic and regional wave-fields, and wave-field animations to reveal both the resolution capabilities of this dense station distribution as well as the enormous spatio-temporal complexity of seismic wave propagation. The time slices and wave-field animations demonstrate the need for dense regional arrays of broad-band stations, such as provided by AlpArray and neighboring networks, to resolve properties of teleseismic wave-fields. Here we present the images of coherent arrivals of direct body and surface waves, multiple body wave reflections, and multi-orbit phases for teleseismic and regional events with moment magnitudes larger than 6 over a time window of at least 2:45 hours.

Spatial observations of the wave-fields illustrate e.g. the decrease in horizontal wavelength from `P` to `S` to surface waves and the way in which they considerably deviate from plane waves, due to heterogeneous earth structures along the path from the source to the array and beneath the regional array itself. Tomographic imaging techniques for the deep structure beneath the regional array have to take this spatio-temporal variability into account and correct for it.

The lateral resolution of the regional broad-band array is however dependent on station density, in this case limited to about $100km$. Only even denser station distributions like those provided by Swath-D suffice to recover wave-fields of short period body and surface waves.

Introduction

Already in 1889 Rebeur-Paschwitz suggested in the first description of the recording of a teleseismic event (at seismometers in Hamburg and Potsdam) to build a global network of identical stations to monitor the world-wide seismicity (Rebeur-Paschwitz, 1889). The ca. 100 Wiechert-seismometers then deployed world-wide until the 1920's were part of such a network, but it was not until the 1960's that the ca. 120 stations of the *World-Wide Standardized Seismograph Network* (`WWSSN`) created the global infrastructure needed, including the data-exchange procedures and station technical capabilities (e.g. Oliver and Murphy, 1971). This allowed for the first time to construct seismogram sections for the whole earth (Müller and Kind, 1976).

https://doi.org/10.5194/se-2020-122
Preprint. Discussion started: 31 July 2020

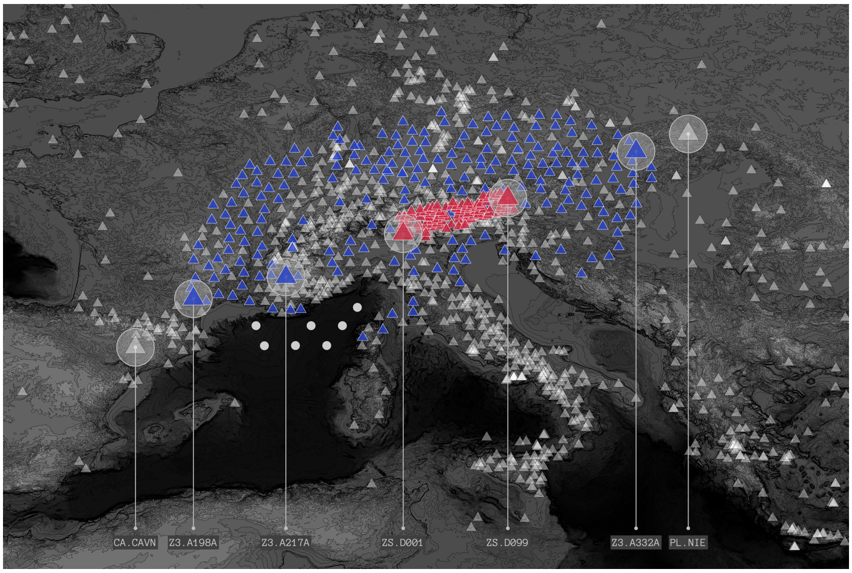

Fig. 1: All available European broadband stations for event No. 1, Taiwan (`C201802061550A`). See Tab. 1 for additional information. Triangles mark individual stations, reference stations for Fig. 2 are prominently marked and labeled. Temporary AlpArray component (`Z3`) in blue, Swath-D (`ZS`) in red, LOBSTER as white circles, all other networks in gray.

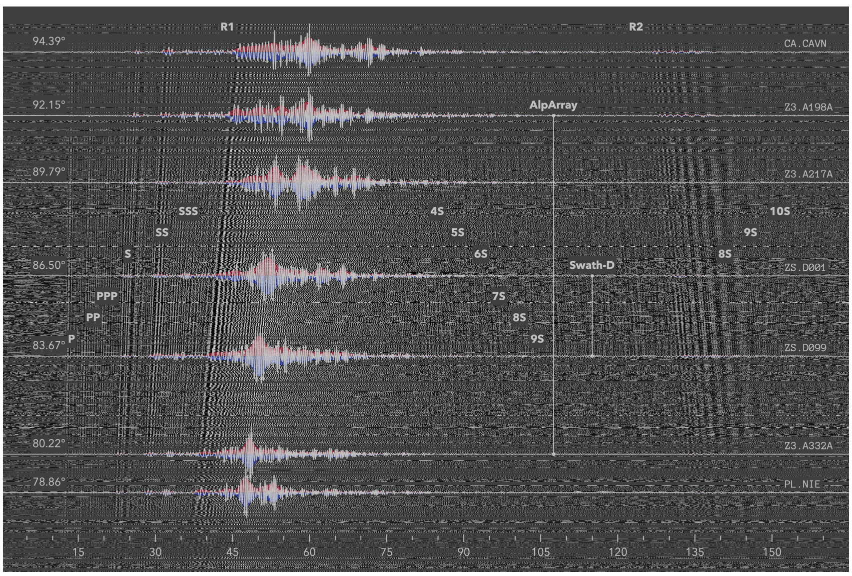

Fig. 2: Seismogram section for event No. 1, Taiwan (`C201802061550A`). Seismograms for reference stations shown in Fig. 1 are plotted on top for comparison at their respective epicentral distances, as labeled on the left. See text for further explanations. Time axis is given in minutes after source time. Selected arrivals are labeled, i.e. `4S` = `SSSS`, etc. Corresponding theoretical travel-times were computed with *TauP* (Crotwell et. al. 1999).

https://doi.org/10.5194/se-2020-122
Preprint. Discussion started: 31 July 2020

The next steps in the observation of seismic signals was the installation of seismic arrays like the Yellowknife Seismological Array (`YKA`) array (Muirhead and Datt, 1976), a system of linked seismometers arranged in a regular geometric pattern (cross, circle, rectangle, etc.), to increase sensitivity. Arrays with broadband seismometers allowing the study of the full wave spectrum radiated by earthquakes became first operational in 1976 (Buttkus et al., 1986). While modelling of the wave propagation has been performed since the 1960's, the advent of better computing facilities in the 1990's allowed for the first time to visualize and study the propagation and interaction of seismic waves inside the earth even with lateral inhomogeneities at high spatial and temporal resolution (Wysession and Shore, 1994, Igel and Weber, 1995, 1996).

On the data side the next big advance came from the simultaneous deployment of hundreds of broadband stations like in the *USArray* (Meltzer et al., 1999) with typical inter-station distances of ca. $70km$ (IRIS Transportable Array, 2003), sometimes supplemented with a rolling scheme. This allowed for the visualization and analysis of waves propagating at the earth's surface as two-dimensional images, in contrast to the classical seismogram analysis (Pollitz, 2008).

Following the decades of high-quality active and passive seismological investigations in the Alps, usually along profiles or over sub-regions of the mountain belt, the European observatory and university research communities joined hands to realize the *AlpArray Seismic Network* (`AASN`) within AlpArray initiative (Hetényi et al., 2018). This major undertaking was only possible through large-scale technical, financial, and organizational coordination: 36 institutions from 11 countries participated in operating the AASN for nearly three years since early 2016. The network is composed of 628 stations in total: 352 permanent and 276 temporary stations on land, and 30 ocean-bottom seismometers in the Ligurian Sea.

In the planning years of the `AASN`, the number of existing permanent stations with accessible data increased by 50%. The corresponding plans for the temporary station sites evolved with time, to ultimately leave no point in the Alps and its surroundings (a $250km$ wide region from the foothills) farther than $30km$ away from a broad-band station (≥ 30 sec lower corner frequency).

In newly covered areas, hexagonal coverage of temporary sites was applied, resulting in an average distance of $52km$ from a site to the neighboring 6 sites, which is tighter and more compact than previous large networks around the world (e.g. USArray's Transportable Array, IberArray). The simultaneous operation of the entire `AASN` officially started on 1st of January 2016 and lasted for 39 months. Each site on land operated for at least 2 years and the majority did for much longer. The full dataset has been recently opened to the entire AlpArray community and will become publicly available on 1st of April 2022. For further details on the `AASN` we refer to Hetényi et al. (2018) and references therein.

The aim of the AlpArray experiment is to image the deep structure of the Alps and to understand the effects of collisional mountain building on a larger scale. The Alps have been the focus of geological research for centuries, with concepts like nappe stacking and subduction first being introduced for the Alpine orogeny (Faccenna et al., 2001, Piromallo and Faccenna, 2004, Vignaroli et al., 2008, 2009, Handy et al., 2010). In order to understand the driving forces of mountain building, the slab geometry and deep crustal structure have to be revealed. Because of the small lateral and highly curved geometries, this remains a challenge. Furthermore, major ambiguities regarding the presence of slab segments, slab gaps, and slab polarity switches might be resolved using advanced seismological imaging techniques and the available dense station coverage (AlpArray Science Plan, 2013, Hetényi et al., 2018).

Here we report on the imaging of the propagation of different wave types across the broader Alpine area, based on the dense deployment of the AlpArray Seismic Network (Molinari et al., 2016, Fuchs et al., 2016, Govoni et al., 2017), neighboring networks of broad-band stations available through EIDA (Clinton et al., 2014), and the AlpArray Complementary Experiment Swath-D (Heit et al., 2017) with inter-station down to as little as $15km$ for Swath-D (cf. Fig. 1). We show single-event seismogram sections, time slices of the wave-fields for specific phase arrivals, and wave-field animations (cf. *Supplementary Materials*) for long time windows to illustrate the capabilities of dense regional and local broad-band arrays. In the main text each event is discussed in detail, identifying relevant phases, and describing observed spatial properties of the wave-field.

Events & Data

Following detailed screening, six representative events have been selected for visualization of seismic wave-fields in the AlpArray region. For three of them (listed in Tab. 1) time slices of the wave-field are discussed in the text. For all six events the studied animations are provided in the supplement. Events for which only animations are presented are given in Tab. 2. All events are described by their corresponding CMT catalog IDs.

The six selected events include both local and teleseismic examples with a variety of different back azimuths to illustrate both the time-dependent evolution of the seismic wave-fields as well as the spatial resolution capabilities of AlpArray and neighboring European broadband seismic networks for the laterally varying properties of the

https://doi.org/10.5194/se-2020-122
Preprint. Discussion started: 31 July 2020

	No. 1	**No. 2**	**No. 3**
CMT ID	`C201802061550A`	`C201801281603A`	`C201610300640A`
Location	Taiwan	Southwest of Africa	Central Italy
Lat., Lon.	$24.0°N$, $121.54°E$	$53.06°S$, $9.95°E$	$42.75°N$, $13.16°E$
Distance	87.11°	98.06°	3.2°
Azimuth	318.8°	0.04°	315.63°
Back Azimuth	58.2°	180.03°	133.44°
Depth	$13.9km$	$12km$	$12km$
Magnitude	$6.37M_W$	$6.51M_W$	$6.59M_W$
Date	2018-02-06	2018-01-28	2016-10-30
Time	15:50:48	16:03:10	06:40:24
Stations	1598	1609	1319

Tab. 1: Three main events. (Distances and azimuths relative to $45°N$, $10°E$.)

	No. 4	**No. 5**	**No. 6**
CMT ID	`C201612251422A`	`C201801250210A`	`C201608240136A`
Location	Southern Chile	Eastern Russia	Central Italy
Lat., Lon.	$43.41°S$, $74.43°W$	$55.54°N$, $166.5°E$	$42.64°N$, $13.22°E$
Distance	115.85°	77.52°	3.31°
Azimuth	51.6°	343.23°	316.45°
Back Azimuth	233.62°	13.36°	134.22°
Depth	$32.8km$	$12km$	$12km$
Magnitude	$7.57M_W$	$6.22M_W$	$6.2M_W$
Date	2016-12-25	2018-01-25	2016-08-24
Time	14:22:38	02:10:38	01:36:36
Stations	1409	1616	1428

Tab. 2: Three supplementary events.

wave-field.

Stations are considered within a region centered around $45°N$ $10°E$, a point in the central Po Basin southeast of Milan, Italy, marking the "center" of the greater Alpine region for the purpose of this study. All relative measures such as event distances and azimuths are given in relation to this point. Data is obtained on a per-event basis for as many stations as possible within a 20° radius, ranging east-to-west from the Black Sea to the northeast Atlantic and north-to-south from central Norway to northern Africa, though the bulk of the station coverage is focused on the Alps.

All available non-restricted European stations with any of LHZ, BHZ, or HHZ channels as well as AlpArray and Swath-D data are downloaded for the selection of exemplary events. The download is facilitated by means of the FDSN web services, yielding approximately between 1300 and 1600 stations from over 60 networks per event, starting at the beginning of 2016. The varying data availability reflects the different operation periods of the temporary components of the station networks. (See list of cited networks in *References*.)

All traces are detrended, instrument response-corrected, band-pass filtered between 100 – $500s$, and resampled to $1Hz$ if necessary. They are technically not perfectly aligned as their start times may be offset from one to another by up to half a sample width due to station effects, but that is negligible as for the purpose of these depictions. Each station's start time is therefore rounded to the nearest integer second for realignment purposes.

https://doi.org/10.5194/se-2020-122
Preprint. Discussion started: 31 July 2020

Solid Earth Discussions

Seismogram Section

Fig. 2 shows an overview of the vertical component dataset for event No. 1 in Taiwan. Several reference traces from stations in the AlpArray, Swath-D, as well as the Italian and German national networks are superimposed onto the section for comparison. The station locations and the extent of the AlpArray and Swath-D temporary networks are shown in Fig. 1. The seismogram section exhibits a multitude of seismic phases, including distinct late arrivals. Sections for the other teleseismic events can be found in the supplementary materials.

To emphasize weaker phases, the traces are individually normalized. They are divided by their respective low-pass filtered envelopes (corner frequency of $5mHz$, 200 sec) and subsequently scaled by a factor of 0.8. This largely confines the data to the target interval of $[-1,\ 1]$, after which it is clipped in the figures.

Samples of all available traces are averaged into small rectangular bins, $0.02°$ by 1 sec in size, with the result being shown as the background of Fig. 2. This means that each bin is usually only comprised of a handful of stations. If enough stations are available per bin, the seismic phases are clearly visible. This is particularly the case for the epicentral distance range between ca. $80° - 92°$ where the dense AlpArray and Swath-D provide a high degree of coverage. If there are only a few traces available per bin, erroneous recordings may determine the average. This can be the case at distances $< 78°$ and $> 92°$ where significantly fewer clear arrivals are visible. E.g. at around $92°$ two traces featuring spurious long-period anomalies across the entire time window are apparent.

As expected, `P`, `S` (cf. Fig. 16 & 17 in the supplementary materials for more detail), and `SS` arrivals are distinctly discernable. In addition, `PP`, `PPP`, and `SSS` are observed within the distance range of the AlpArray. A number of other early arrivals are visible between `PPP` and `S`, as well as between `SSS` and `R1`, though their identification is not immediately obvious, as there exists a set of higher order `P` and `S` reflections or `S`-to-`P` conversions at $410km$ and $660km$ with similar arrival times that would be expected to superimpose at this point.

The `R1` arrival itself is very strong, starting at around 40 min. Once the surface wave coda diminishes after ca. 70 min, several phases are entering the array from the opposite direction, as indicated by an arrival time decreasing with distance. They are only imaged clearly in the distance range of AlpArray, outside of which they quickly become faint and difficult to identify as a result of the significantly smaller station density outside of the `AASN`, at the top and bottom of Fig. 2. Examples of phases visible in this time period include `4S`, `5S`, and `6S` as well as their related higher order `P` reflections.

At about 130 min the Rayleigh wave `R2` can be seen entering from the southwest. Higher frequencies are significantly reduced due to the longer travel path as compared to the direct arrival `R1`, resulting in a coherent long-period wave-form band stretching out over almost 15 min.

After `R2` a number of body wave arrivals with more than one around-the-globe orbit enter again from the northeast. They are visible in the time range between ca. 145 min and 160 min. These include `8S`, then `9S`, followed by even higher order `S` reflections and their respective closely related `P` phases. To the best of our knowledge these are the first direct observations of such phases in single-event datasets.

Fig. 2 shows that also small and late arrivals can be detected by a dense array using recordings of just one event.

Animations

The lateral variability of the wave-fields cannot be adequately represented via a seismogram section, hence a more spatial view of the data is needed, as for example in Fig. 3 – 6, 8 – 12, and 14.

In order to make use of the full dynamic range of the color scale at any time, we apply the same time-dependent normalization of the seismograms at each station as for the section (Fig. 2). Additionally, the traces are band-pass filtered down to a minimum period of 20 sec to ensure a good signal-to-noise ratio and coherent phase arrivals given the available stations density. The traces are cut to a length of 220 min starting 10 min before source time for local events and to a length of 165 min starting at source time for teleseismic events.

Note that the only quality control metric that was used, is a basic percentage threshold regarding the number of samples that must be present in the individual traces for them to be used. Data from stations missing more than 10% of their samples are discarded.

The animations are rendered within a rectangular region from $54°N\ 4°W$ (Great Britain) in the top-left to $34°N\ 26°E$ (Greece) in the bottom-right, covering the Alpine region and its surrounding area. This selection includes most stations available within the aforementioned $20°$ circle. The playback speed is 30 times real-time.

A vertical bar above the unweighted reference trace at the bottom of the animations indicates the point in time at which the wave-field is shown. The station from which the reference trace was taken is indicated by a triangular marker. The reference trace is displayed on top of its weighting envelope. The size of the circular station markers are proportional to their current absolute vertical ground velocity and the color encodes the direction of displacement, positive as red and negative as blue. The top right corner features an arrow indicating the azimuth of the direct arrivals. Small circles around the epicenter are included as faint lines at $2°$ increments to indicating the

https://doi.org/10.5194/se-2020-122
Preprint. Discussion started: 31 July 2020

approximate shape of the expected wave-fronts for the case of a spherically symmetric earth. Spatial distortions of the wave-field from these theoretical wave-fronts indicate the degree to which arrivals locally deviate due to lateral inhomogeneities encountered along the paths to the stations.

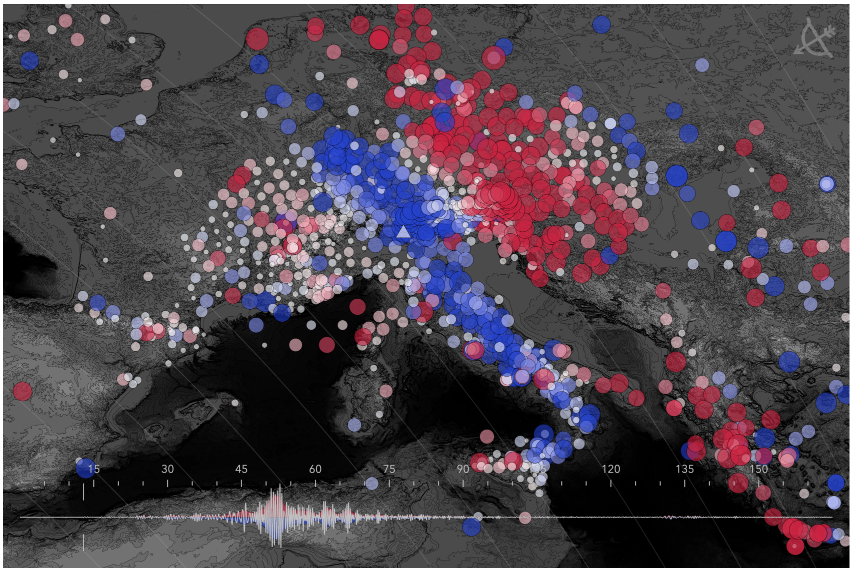

Fig. 3: `P` arrivals at 00:12:55 after source time. Reference trace at `ZS.D001` marked with a white triangle. Event No. 1, Taiwan (`C201802061550A`).

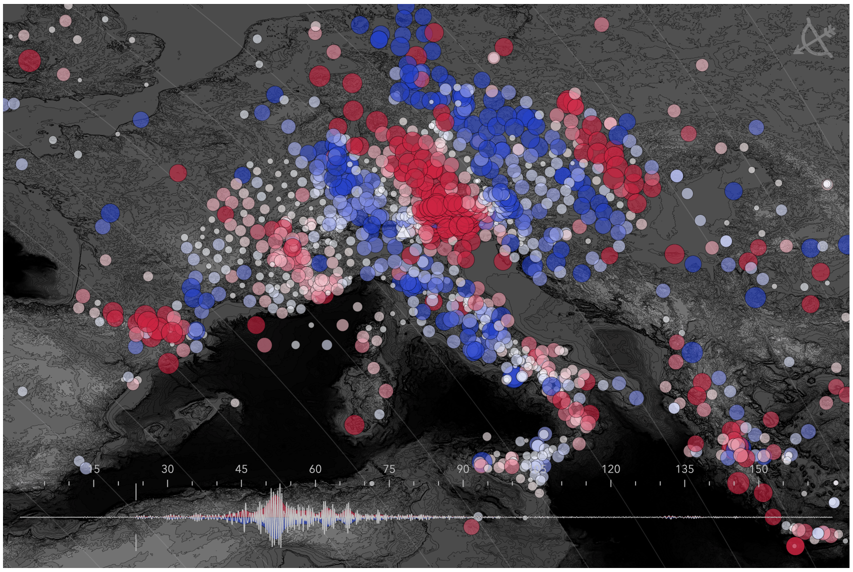

Fig. 4: `S` arrivals at 00:23:35 after source time. Reference trace at `ZS.D001` marked with a white triangle. Event No. 1, Taiwan (`C201802061550A`).

https://doi.org/10.5194/se-2020-122
Preprint. Discussion started: 31 July 2020

Solid Earth
Discussions
Open Access
EGU

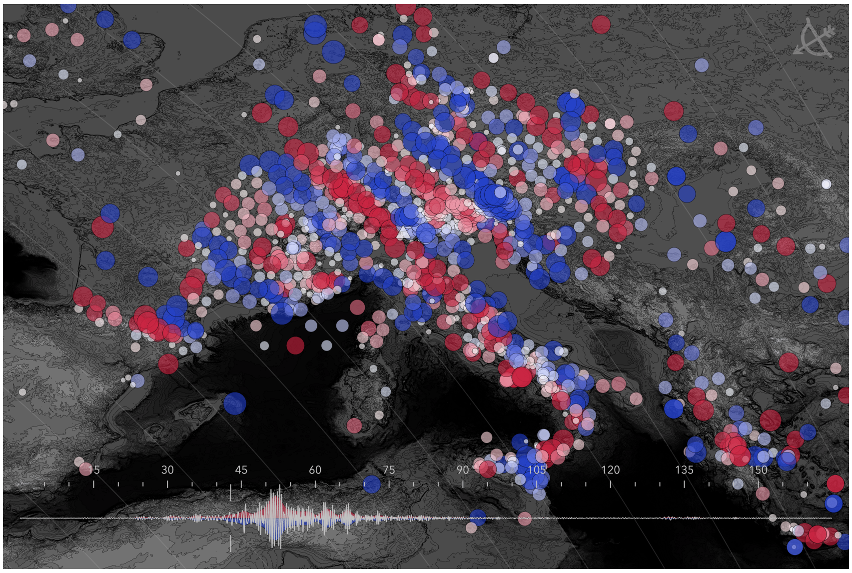

Fig. 5: `R1` arrivals at 00:42:50 after source time. Reference trace at `ZS.D001` marked with a white triangle. Event No. 1, Taiwan (`C201802061550A`).

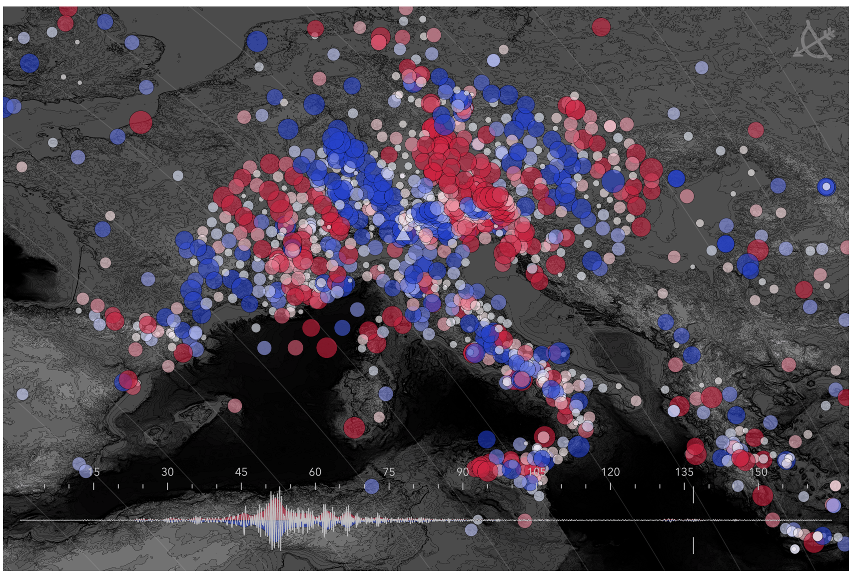

Fig. 6: `R2` arrivals at 02:16:50 after source time. Reference trace at `ZS.D001` marked with a white triangle. Event No. 1, Taiwan (`C201802061550A`).

Discussion

(1) Taiwan (`C201802061550A`)

We start the discussion of the animations with an event located to the east of the network. It took place in Taiwan, ca. 87° away from the center of the Alps, with a moment magnitude of M_w 6.4 (cf. Tab. 1). For this event we describe the full variety of arriving waves that are visible due to the dense station coverage. The animation starts at the source time, showing some random but coherent wavelets of unrelated phases arriving from all directions

https://doi.org/10.5194/se-2020-122
Preprint. Discussion started: 31 July 2020

Solid Earth Discussions

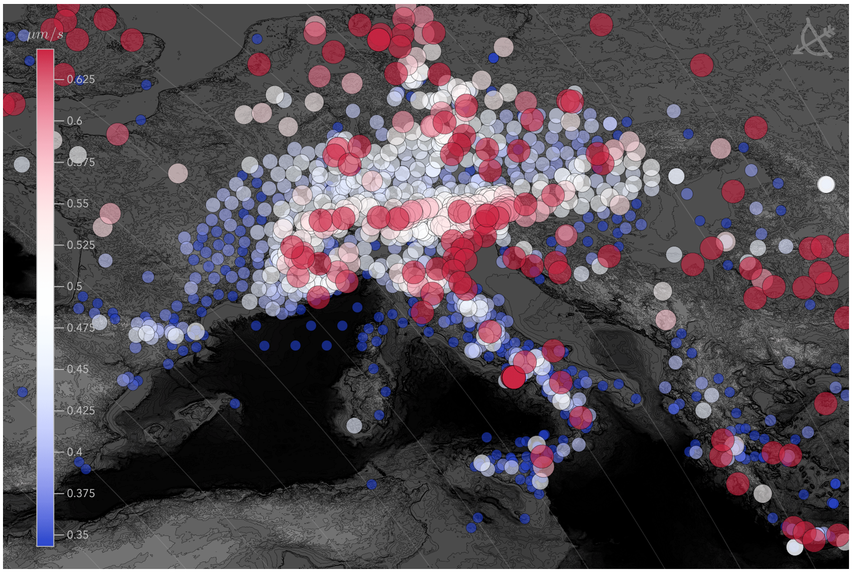

Fig. 7: Standard deviation of vertical ground velocity over a 2:45 *hour* period, starting at source time. Event No. 1, Taiwan (`C201802061550A`).

in the Alps.
Note that the small circles indicated in Fig. 3 – 7 seem to suggest the event being located southwest of the observed region due to their curvature. This is not the case, it is merely an artifact of the projection that they appear to curve away from the source. The source itself is furthermore located at a latitude slightly lower then the bottom edge of the figures, instead of being located in the northeast as the wave's azimuth might suggest, again an artifact of the projection.
The direct `P` phase arrives after about 12 *min* (cf. Fig. 3), coming in from the north-east. Remarkably, the horizontal wavelength varies considerably throughout the `P` arrival, as can be seen in Fig. 3, where the earlier negative part of the phase appears to cover a horizontal width of about 4°, followed by a positive branch of roughly 8°. This can be in part due to a source effect overprinting the propagation effects, particularly as the event has a relatively long half-duration of 3.7 *sec*, but given the dominant period of > 20 *sec*, it is more likely an example of dispersion in body waves.
The following `PP` phase arrives at ca. 15 *min*, showing similar dispersion, albeit less pronounced. Its horizontal wavelength is about 3°. For the `PPP` arrival at ca. 17 *min*, the dispersion is no longer evident, and the horizontal wavelength further reduced to about 2° (not shown in figures, cf. animation). The wave-fronts of these phases are well aligned with the small circles, showing only weak lateral deformation, possibly due to relatively simple upper-mantle structure in northeast Europe. Overlapping higher order `P` arrivals and converted phases follow, evidenced by the variations in horizontal propagation velocity and wavelength of the wave-fronts seen in the animation from 17 *min* until the arrival of `S` at ca. 23 *min* (cf. Fig. 4). `S` has a horizontal wavelength of about 3°, with its wave-front being mostly aligned with the small circles as well. A number of converted phases (`PS`, `PPS`, etc.) with horizontal wavelengths of roughly 2° follow immediately after. They show slight deformations, in particular within Swath-D.
The `SS` phase arrives at about 30 *min*. The wave-front is visibly deformed, again with a small delay showing in the Central Alps as seen in the previous example. `SSS` and other higher order body wave arrivals before `R1` are again heavily interfering and severely deformed, thus cannot be uniquely separated.
The surface wave `R1` reaches the array at ca. 43 *min* (cf. Fig. 5), but there is no clear distinction to the multitude of preceding phases, as the surface wave arrival has a rather emergent characteristic. Its horizontal wavelength is small at less than 2° and its horizontal velocity is the smallest of all arrivals. Its coda dominates the signal for about 30 *min*, developing into an incoherent high frequency signal after ca. 52 *min* when periods shorter than about 20 *sec* start to become prevalent. They cannot be properly imaged by the available station density, with only few deformed but coherent wavelets again visible within the denser Swath-D.
At 80 *min*, the coda has sufficiently diminished in amplitude so that higher order body wave phases are again

https://doi.org/10.5194/se-2020-122
Preprint. Discussion started: 31 July 2020

discernable. The picture is much less clear in comparison with the previously discussed event, but a number of phase bundles arriving from the west are still identifiable. They show significant deformation as a result of their long travel path.
At about 130 *min* the returning surface wave `R2` emerges over the array from the southwest. It again lacks the high frequencies of `R1` (cf. Fig. 7) and exhibits strong dispersion over the course of its arrival, which lasts until ca. 145 *min*.
Note that time slices of this kind can also be useful to spot either polarity or timing errors in individual stations. Both the figures shown here and the animations clearly point out a few out-of-phase traces, particularly during long wavelength arrivals such as `P`. Fig. 3 shows a few cases near Venice (red), over the Dinarides (blue), and in southern Germany (blue), for example.
Fig. 7 gives the standard deviation of the unnormalized traces. It does not decrease with distance, it shows instead a prominent amplification in the region of the Alps and northern Italy, as well as similar perturbations over Sicily and in central Italy. Overall these anomalies are less pronounced here than compared to the following event (cf. Fig. 13), with a maximum amplification by a factor of about 1.5 versus > 2 for the next one, as the variations in surface wave amplitudes are more chaotic.
Such standard deviations can serve as a proxy indicator for the deformation of local amplitudes, either due to scattering outside of the array or because of shallow and deep inhomogeneities beneath the stations. It has been shown that between 40 – 60% of amplitude residuals can be explained by surficial sediment layers alone (Weber, 1994). To examine these effects in more detail, it might be useful to in the future look at accumulated standard deviations from a broader collection of events, covering the complete azimuth range, to suppress any deformations that occured outside of the observed region.

(2) Southwest of Africa (C201801281603A)

For the second event discussed here, the source is located in the South Atlantic, southwest off the coast of Africa, ca. 98° away from the center of the Alps, with a moment magnitude of M_w 6.5 (cf. Tab. 1).
The animation starts with ca. 14 *min* of ambient background signal to be observed before any phases arrive. It is mostly comprised of random noise and appears incoherent, though some small-scale coherent wave-fields do occasionally emerge. They are particularly distinct within the Swath-D network, where a number of compact wavelets unrelated to the event can be seen entering from various directions, either caused by anthropogenic sources or small-scale local seismic activity.
Fig. 8 shows the `P` arrival reaching the Alps at ca. 14 *min*. It exhibits the longest horizontal wavelength of all phases with about 6° – 7°. Interestingly, the expected transition from `P` to $\mathtt{P_{diff}}$ occurs at about the reference station at the center of the displayed region (cf. Fig. 8 – 12). The wave-front seems largely aligned with the theoretical wave-front (cf. thin gray lines in Fig. 8). It is closely followed by `PP` and `PPP` at ca. 18 *min* and 20 *min* respectively, which already show a significantly reduced horizontal wavelength of about 4°, due to the shallower angle formed between their travel paths and the surface. They are also largely unaffected by distortions and appear laterally rather coherent (not shown in figures, cf. animation).
Several higher order `P` reflections arrive from about 20 *min* until the arrival of the `S` wave at ca. 27 *min* (cf. Fig. 9). They appear highly influenced by lateral inhomogenous structure along their paths, being not as clear as the lower order multiples, not always being visible across the full width of the array, and sometimes strongly deviating from the theoretical spherical wave-fronts (cf. animation). The `S` arrival (Fig. 9) shows some distortion and shorter horizontal wavelength compared to all previous phases of just about 3°. Also, the horizontal propagation velocity is considerably lower. It is directly followed by a number of converted phases (`PS`, `PPS`, etc.) which are again only well resolved in parts of the array. The `SS` phase is clearly visible as well with similar wavelength and velocity as `S` at ca. 33 *min*. It is immediately followed by `PSS` at about 34 *min*. `SSS` and other higher order body wave phases arriving before `R1` are heavily interfering with one another and cannot be uniquely separated, though their superposition can still be observed as a strongly distorted and fragmented wave-field before the Rayleigh wave. These phases are notably more sensitive to 3D structure, sometimes reaching the array at an oblique angle compared to the theoretical great circle path, which is particularly obvious within the Swath-D network.
The surface wave `R1` reaches the array at ca. 48 *min* (cf. Fig. 10). The Rayleigh wave train is dominated by periods of about 30 *sec* to 60 *sec*. It exhibits the smallest horizontal wavelength (less than 2°) and lowest velocity of all arrivals. Its coda dominates the signal for almost half an hour. Due to the high frequencies present in the coda and the interference of scattered waves, the wave-field cannot be properly resolved with even the inter-station distances of AlpArray. Only within the Swath-D there are some highly scattered wave-fronts occasionally visible. This shows the importance of dense arrays for understanding the spatial characteristics of real-world seismic wave-fields. Given the fact that at least two stations are needed within a given wavelength to resolve it, whichever

https://doi.org/10.5194/se-2020-122
Preprint. Discussion started: 31 July 2020

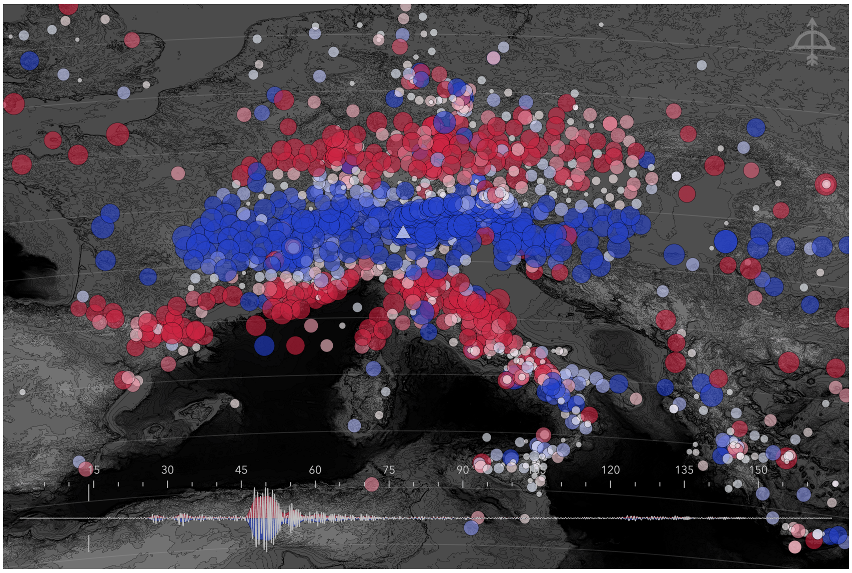

Fig. 8: `P` arrivals at 00:14:00 after source time. Reference trace at `ZS.D001` marked with a white triangle. Event No. 2, Southwest of Africa (`C201801281603A`).

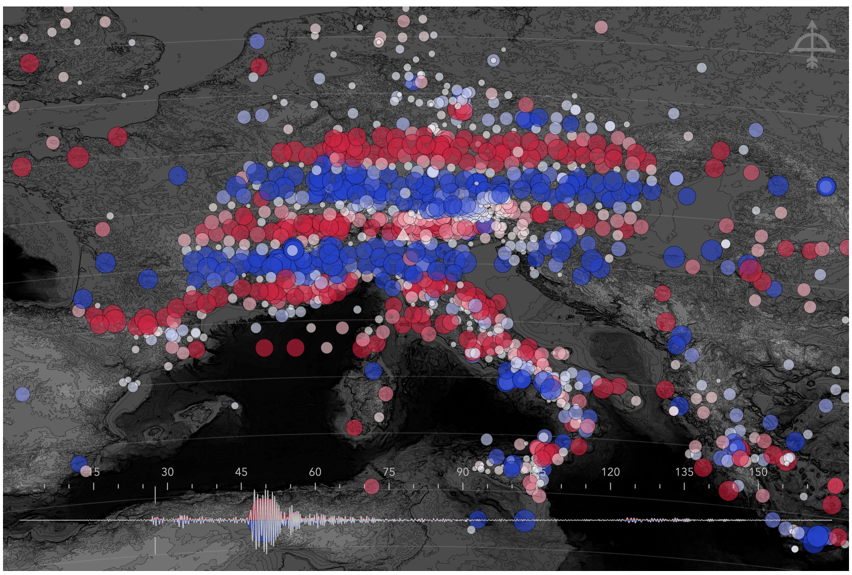

Fig. 9: `S` arrivals at 00:27:30 after source time. Reference trace at `ZS.D001` marked with a white triangle. Event No. 2, Southwest of Africa (`C201801281603A`).

direction the propagation might be, means that about double the station density available in the AlpArray today would be required to make meaningful progress in spatially imaging surface wave codas in particular.

After the surface wave coda has diminished, several higher order reflections are seen after ca. 73 *min* arriving from the north, having taken the opposite path around the earth as the prior direct arrivals. They are usually comprised of a bundle of similar phases arriving in close succession, having a fixed number of `S` reflections and a varying number of `P` reflections. Fig. 11 shows a prominent example of such a bundled arrival at ca. 87 *min*, starting with `6S`, `P6S`, and up to a dozen added `P` reflections following within the next 2 *min*.

For the next ca. 40 *min* other late arrivals appear from both the north and the south, often several at the same

https://doi.org/10.5194/se-2020-122
Preprint. Discussion started: 31 July 2020

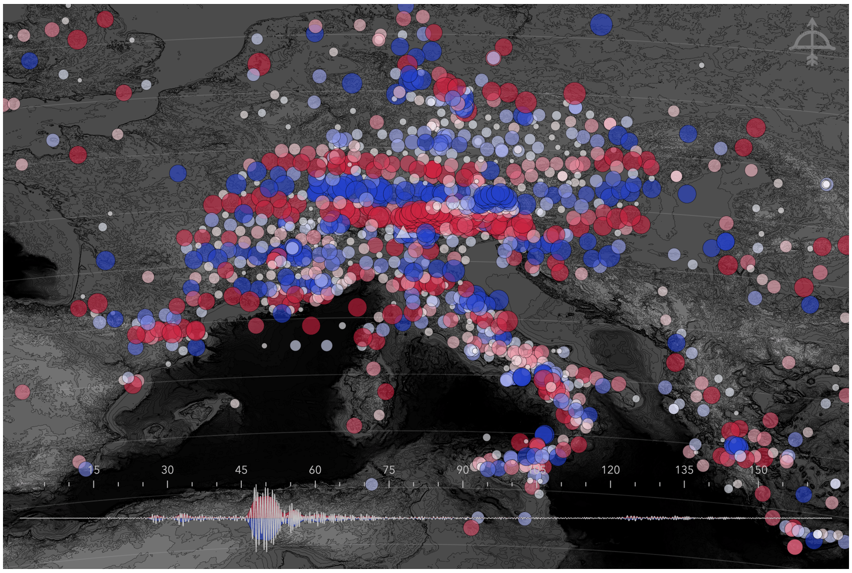

Fig. 10: `R1` arrivals at 00:48:00 after source time. Reference trace at `ZS.D001` marked with a white triangle. Event No. 2, Southwest of Africa (`C201801281603A`).

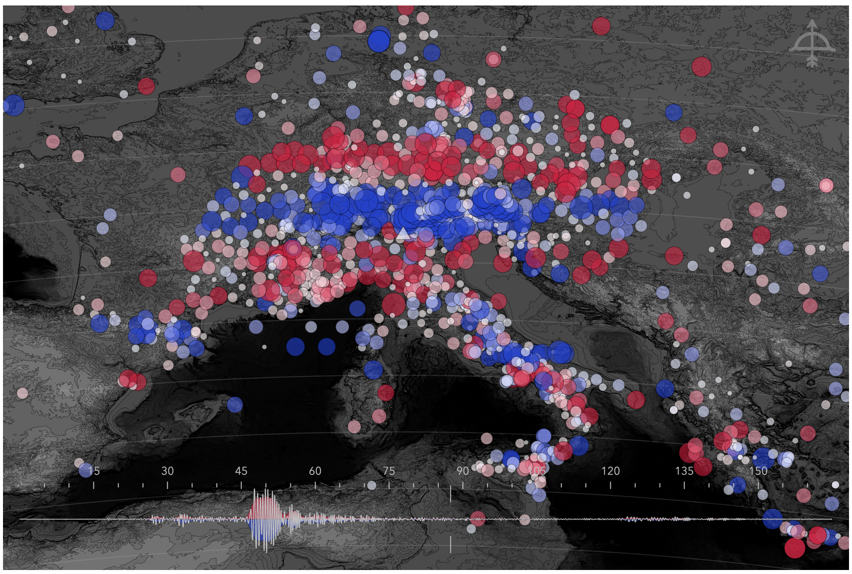

Fig. 11: `6S`, `P6S`, and related arrivals at 01:27:30 after source time. Reference trace at `ZS.D001` marked with a white triangle. Event No. 2, Southwest of Africa (`C201801281603A`).

time, resulting in very scattered wave-fronts. Though largely incoherent, the overall wave-field is still perceptibly different compared to the random noise at the beginning of the animation.
At about 123 *min* the returning surface wave `R2` also reaches the array. As a result of anelastic damping it lacks high frequencies compared to `R1` (cf. Fig. 18 in the supplementary materials). It exhibits strong dispersion as shown by the dramatic increase in wavelength over the course of its arrival.
Fig. 13 gives an overview of the standard deviation of the original (i.e. before normalization) traces over the time period of the animation. Surprisingly, the standard deviation that is dominated by the Rayleigh wave `R1` does not

https://doi.org/10.5194/se-2020-122
Preprint. Discussion started: 31 July 2020

Solid Earth
Discussions
Open Access

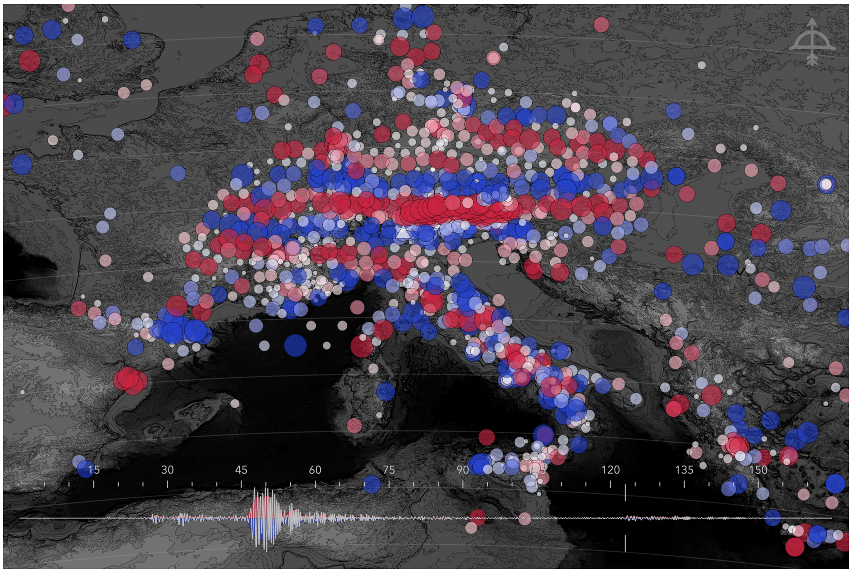

Fig. 12: `R2` arrivals at 02:03:00 after source time. Reference trace at `ZS.D001` marked with a white triangle. Event No. 2, Southwest of Africa (`C201801281603A`).

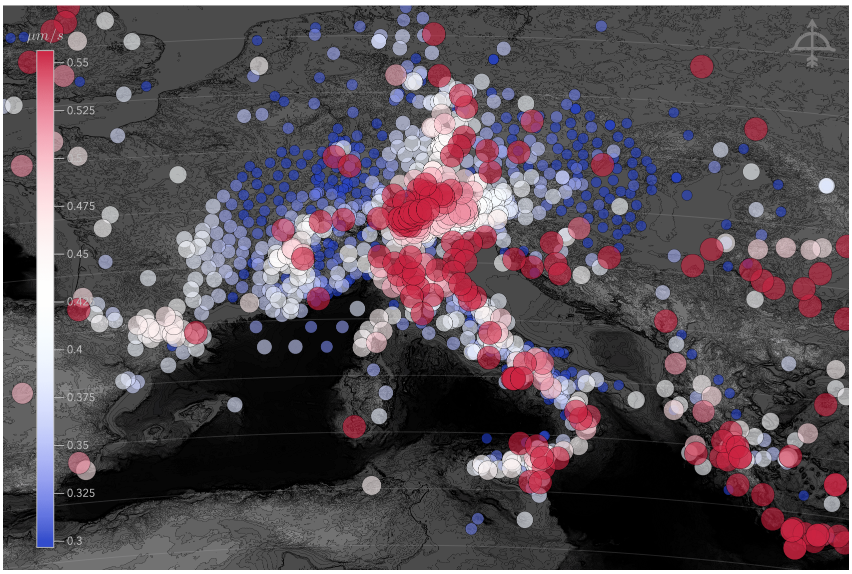

Fig. 13: Standard deviation of vertical ground velocity over a 2:45 *hour* period, starting at source time. Event No. 2, Southwest of Africa (`C201801281603A`).

decrease with distance. Instead, it shows a prominent amplification in the region of the central Alps and northern Italy, on Sicily and in the region of the central Italian volcanic fields. A positive anomaly is visible within the inner arc of the western Alps. Lower values might correspond to thinner crust, e.g. in the Black Forest and the western end of the Pannonian Basin. This points to the importance of local heterogeneity of the crust and upper mantle structure as well as potential focusing and defocusing effects induced outside of the observed region for Rayleigh wave amplitudes.

https://doi.org/10.5194/se-2020-122
Preprint. Discussion started: 31 July 2020

Solid Earth
Discussions
Open Access

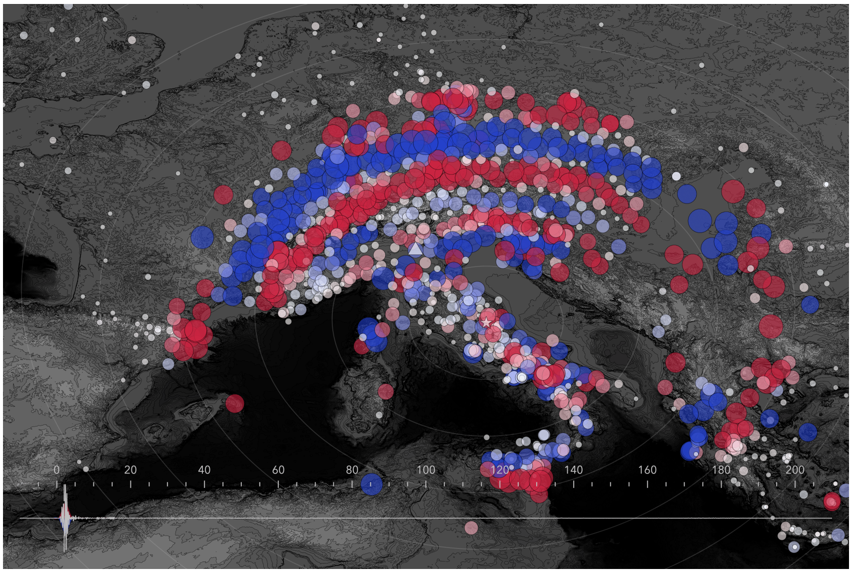

Fig. 14: Wave-field at 00:02:00 after source time. Reference trace at `Z3.A313A` marked with a white triangle. Epicenter marked with a white star. Event No. 3, Central Italy (`C201610300640A`).

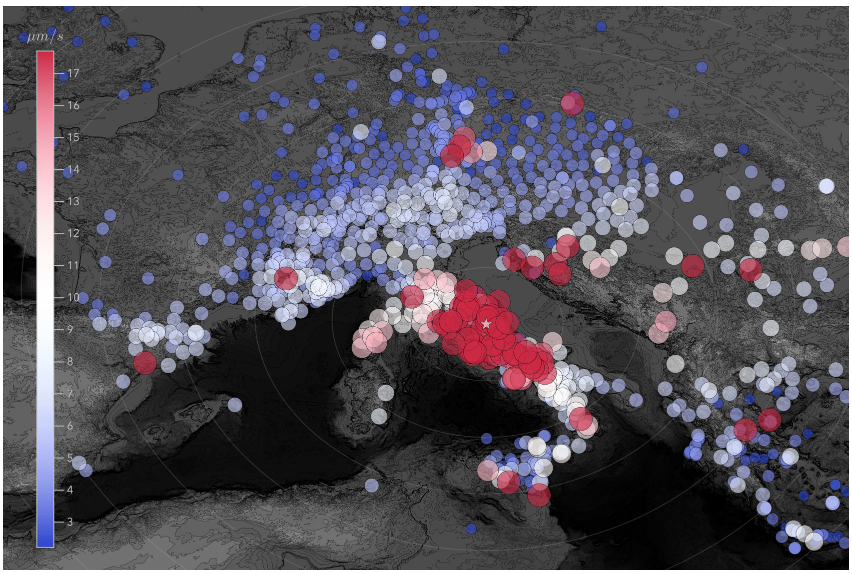

Fig. 15: Standard deviation of vertical ground velocity over a 3:40 *hour* period, starting at 10:00 *min* before source time. Epicenter marked with a white star. Event No. 3, Central Italy (`C201610300640A`).

(3) Central Italy (`C201610300640A`)

For the purposes of local events such as this one, the animation begins at 10 *min* before source time. The event has a moment magnitude of M_w 6.6, with the epicentre merely 3° away from the center of the array, well within the available station distribution. This is a very unique setting, allowing for direct observation of the wave-field in the source region.

https://doi.org/10.5194/se-2020-122
Preprint. Discussion started: 31 July 2020

The noise visible before the event is similar to the previous two examples, though the resolution of small-scale coherent patterns suffers, particularly from to the lack of the Swath-D network which was not yet deployed at the time of this event (October 2016).
As a result of the close proximity to the source, all direct arrivals are seen in close succession, quickly propagating out of the array. At about 1 *min* both `P` and `S` phases pass over the main Alpine Arc, with the Rayleigh wave `R1` just reaching the southern part of the Po Basin. The dramatically decreased arrival angle of the body wave phases as compared to the teleseismic examples also leads to a significantly reduced horizontal wavelength of less than 2° for `P`, as well as a much slower horizontal propagation velocity. At the periods considered, deformations of the wave-front are almost not discernable for such short ray paths as seen here, because accumulated delays / advances induced by crustal structure are yet too weak to be distinctly resolved in the spatial domain by the available station density.
Fig. 14 shows the wave-field at 2 *min*. `P` has already propagated beyond the observed region, while `S` just reaches the northern and western edges of the AlpArray network. `R1` approaches the south-eastern end of the Alpine Arc. Unlike the body waves, its horizontal wavelength and velocity remain unaffected by the close proximity to the source, because its ray path is bound to the surface, thus leading to a constant angle of incidence regardless of the distance. The coda is very short and at about 5 *min* the Rayleigh wave is no longer visible as well.
After `R1` the data quickly returns to noise, as there are no phases reaching the array until the arrival of waves that have completed a full global orbit. Noise remains prevalent for about 1 *hour*. The first returning phases are seen at ca. 62 *min*, though they do not appear as distinct wave-fronts but rather as highly scattered and deformed wavelets. This is expected as the superposition of arrivals collapsing back into the source from practically every direction after circling the entire earth is bound to be strongly affected by global 3D structure and the earth's ellipticity. This effect would probably be even more pronounced for larger magnitude earthquakes, though none occured during operation of the AlpArray network.
The arrival of scattered returning higher order reflections continues for over 100 *min*. At some points the wave-field does coalesce into a semi-coherent ring-like wave-front (e.g. at 90 *min*, likely `10P2S` and higher), but most of the time it is rather fragmented, sometimes even seemingly forming standing waves between simultaneous arrivals from opposite directions (e.g. at 110 *min*, likely `6S` and related `P` reflections).
The returning Rayleigh wave `R2` is seen from ca. 168 *min* onwards. It first enters from the north as an almost planar, surprisingly intact wave-front, slowly shifting to a south-easterly direction of propagation over the next 2 *min*. Shortly after, `R2` arrivals from the south and west become apparent as well and the wave-field grows very complex again. The dispersive Rayleigh wave coda dominates for the next ca. 20 *min*.
Besides potential 3D structure and a cumulatively faster propagation velocity along the path over the poles, the delay in `R2` arrivals from the east and west is also likely aided by the ellipticity of the earth and the appreciably shorter pole-to-pole radius. The east-to-west propagation path is about $70km$ longer, resulting in an expected delay of about 24 *sec* for periods around 50 *sec*. It can therefore not be the sole reason for the observed behavior, particularly as it would not introduce any incoherency into the wave-field by itself.
The standard deviation shown in Fig. 15 is dominated by the effect of geometric spreading of the Rayleigh wave amplitudes, quickly dropping off with distance to the source. A few discernable features are visible, such as slightly elevated amplitudes over the Alpine Arc, the Po Basin, and Sicily. A sharp discontinuous drop-off in amplitude occurs in Central Italy just north of Florence, where the Apennines bend westward, forming the southern / south-western border of the Po Basin.

(4) Southern Chile (`C201612251422A`)

As an example of a wave-field from a higher magnitude source we show an event in Southern Chile from 2016 in the supplementary materials. With a moment magnitude of ca. M_w 7.5 it is significantly stronger than the previous examples. It is also located furthest away at a distance of about 115°.
The observed phase arrivals are unanimously stronger and very clearly visible, including late phases arriving even after `R2` from ca. 135 *min* on. Especially the quality of phases after the second Rayleigh wave arrival is unprecedented as can be seen among the examples shown in this paper.
The standard deviation (Fig. 21) shows several similar features in Central Italy and Sicily as the previous events. In the Po Basin a clear negative anomaly emerges. The image is dominated by a clear west-to-east stripe of positive anomalies over the Alpine Arc, not dissimilar to the north-to-south reaching anomaly observed for event No. 2 (cf. Fig. 13). These features are likely induced by scattering outside the array (Kolínský et al., 2019).

https://doi.org/10.5194/se-2020-122
Preprint. Discussion started: 31 July 2020

(5) Eastern Russia (C201801250210A)

An additional example of an event with moment magnitude ca. M_w 6 at a distance of about 77° is provided in the supplementary materials. The wave-front reaches the array roughly from the north, featuring similar clearly visible phase arrivals as the events in the South Atlantic and Taiwan.
R2 is slightly less prominent as a result of its longer travel path and the subsequently more pronounced attenuation. It therefore lacks the clear indicators of dispersion that can be observed in the other cases.
The standard deviation (Fig. 22) shows comparable features to the South Atlantic event with a strong anomaly in the Central Alps, Po Basin, and the volcanic regions of Southern Italy.

(6) Central Italy (C201608240136A)

The last example shown in the supplementary materials is a second local event in Central Italy, almost identical to example No. 3. It also includes two visible aftershocks at ca. 58 *min* and 152 *min*. R2 arrives again first from the north, corroborating the shorter travel path over the poles as a probable contributing factor for the east-west delay.

Conclusions

With the advent of large-aperture, dense, regional broad-band arrays, the full complexity of seismic wave-fields can be imaged. Animations in particular can provide an adequate impression of seismic wave-fields, well suited for a variety of purposes from educational ones to advanced research. A dynamic gain control allows to image stronger direct teleseismic body and surface wave arrivals as well as multiply reflected and multi-orbit waves. Phases like 9S, 10S, etc. are detectable using recordings of just one event.
It becomes obvious that teleseismic wave-fronts deviate strongly from plane waves. This holds for direct P and S waves and even more for later arrivals. This observation was the basis for the mis-location vectors of arrays, enabling to determination the actual location of unknown events using arrays (Krüger, Weber, 1992).
It is interesting to note the decreasing horizontal wavelength from first arriving P waves to the fundamental Rayleigh mode, despite longer periods being more prominent in the surface wave train. Recordings of large and dense arrays are necessary to understand these wave-fields and consequently sparse spatial sampling may lead to severe aliasing that can not be overcome by any imaging techniques. That means large and dense regional arrays represent a prerequisite to measure properties of teleseismic wave-fields.
It remains however a challenge to extract information on the local structure, because the wave-fields are strongly influenced by the structure outside of the array. This is demonstrated by considering the standard deviation of the seismograms, which is mainly sensitive to the large amplitudes of the fundamental Rayleigh mode. There is a strong amplification especially in the Alpine area by at least a factor of about two that completely overprints the expected decay of amplitudes with epicentral distance. Furthermore, amplifications in narrow bands often oriented almost parallel to the propagation direction are frequently observed, pointing to interference of the direct surface waves with surface waves forward scattered at lateral heterogeneity outside of the array. Amplitude variations due to inhomogeneities in the source region can reach a factor of up to 10 over a distance range of 10° at tele-seismic distance (Weber, 1990). For 3D modelling including anisotropy and even stronger effects see Kendall and Thomson (1993).
Because of the lateral extent of the regional array, it also covers the source region for some events. Therefore, wave-fields in source regions as well as wave propagation over regional distances may be directly observed without spatial gaps. Also, smaller events can be detected and source parameters can be determined using a large number of recordings at close distances.
In addition to large regional arrays, very dense deployments of broad-band stations like the Swath-D can help to reduce the shortest resolvable wavelength considerably further, however only in smaller regions. Wave-fields of short period and scattered waves can be adequately measured by dense deployments as provided by the Swath-D network. For example, coherent wave-fields in the surface wave coda wave train can only be detected by Swath-D but not the rest of the regional array.
Finally, it is worth mentioning that the deployment of large, dense regional arrays points also to the importance of a consequent quality control. In particular, timing errors as well as false information on the sensors' properties have to be detected and corrected in order to use the full potential of the arrays, including amplitude information. The obtained data set will be the basis for an improved understanding of seismic wave-fields in a strongly heterogeneous region as well as of the deep structure of the Alpine orogen.

References

AlpArray Science Plan, 2013, `http://www.alparray.ethz.ch/export/sites/alparray/.galleries/dwn-experiments/AlpArray-Dokus.pdf`

Buttkus et al., *Ten Years of the Gräfenberg Array, Defining the Frontiers of Broadband Seismology*, Geologisches Jahrbuch, Band E 35, 1986, ISBN978-3-510-96051-4

Clinton, J., Hanka, W., Mazza, S., Pederson, H., Sleeman, R., Stammler, K., Strollo, A., van Eck, T., *EIDA: The European Distributed Data Archive for Seismology*, Conference on Earthquake Engineering and Seismology, 2014

Crotwell, H. P., Owens, T. J., Ritsema, J., *The TauP Toolkit - Flexible Seismic Travel-Time and Ray-Path Utilities*, Geophysical Journal International, Vol. 110, Issue 3, 501 – 517, 1999. 10.1785/gssrl.70.2.154

Dziewonski, A. M., T.-A. Chou and J. H. Woodhouse, *Determination of Earthquake Source Parameters from Wave-Form Data for Studies of Global and Regional Seismicity*, J. Geophys. Res., 86, 2825 – 2852, 1981. 10.1029/JB086iB04p02825

Ekström, G., M. Nettles, and A. M. Dziewonski, *The Global CMT Project 2004 – 2010: Centroid-Moment Tensors for 13 017 Earthquakes*, Phys. Earth Planet. Inter., 200 – 201, 1 – 9, 2012. 10.1016/j.pepi.2012.04.002

Faccenna, C., Becker, T. W., Lucente, F. P., Jolivet, L., Rossetti, F., *History of Subduction and Back Arc Extension in the Central Mediterranean*, Geophysical Journal International, Vol. 145, 809 – 820, 2001, 10.1046/j.0956-540x.2001.01435.x

Faccenna, C., Piromallo, C., Crespo-Blanc, A., Jolivet, L., Rossetti, F., *Lateral Slab Deformation and the Origin of the Western Mediterranean Arcs*, Tectonics, Vol. 23, 2004, 10.1029/2002TC001488

Fuchs, F., Kolínský, P., Gröschl, G., Bokelmann, G., Govoni, A., *AlpArray in Austria and Slovakia: Technical Realization, Site Description and Noise Characterization*, Advances in Geosciences, Vol. 43, 1 – 13, 2016

Govoni, A., et al., *AlpArray-Italy: Site Description and Noise Characterization*, Copernicus Publications, Vol. 43, 2017, 10.5194/adgeo-43-39-2017

Grapenthin, R., Freymueller, J. T., *The Dynamics of a Seismic Wave-Field - Animation and Analysis of Kinematic GPS Data Recorded During the 2011 Tohoku-oki Earthquake, Japan*, Geophysical Research Letters, 2011. 10.1029/2011GL048405

Handy, M. R., Schmid, S. M., Bousquet, R., Kissling, E., Bernoulli, D., *Reconciling Plate-Tectonic Reconstructions of Alpine Tethys with the Geological–Geophysical Record of Spreading and Subduction in the Alps*, Earth-Science Reviews, Vol. 102, 121 – 158, 2010, 10.1016/j.earscirev.2010.06.002

Heit, B., Weber, M., Tilmann, F., Haberland, C., Jia, Y., Pesaresi, D., *The Swath-D Seismic Network in Italy and Austria*, 2017, 10.14470/MF7562601148

Hetényi, G. et al., *The AlpArray Seismic Network: A Large-Scale European Experiment to Image the Alpine Orogen*, Surveys in Geophysics, Vol. 39, 1009 – 1033, 2018, 10.1007/s10712-018-9472-4

Igel, H., Weber, M., *P-SV Wave Propagation in the Earth's Mantle Using Finite Differences: Application to Heterogeneous Lowermost Mantle Structure*, Geophysical Research Letters, Vol. 23, 415 – 418, 1996

Igel, H., Weber, M., *SH-Wave Propagation in the Whole Mantle Using High-Order Finite Differences*, Geophysical Research Letters, Vol. 22 (6), 731 – 734, 1995

IRIS Transportable Array, *USArray Transportable Array*, International Federation of Digital Seismograph Networks, Dataset / Seismic Network, 2003, 10.7914/SN/TA

Kendall, J.-M., Thomson, C. J., *Seismic Modelling of Subduction Zones with Inhomogeneity and Anisotropy: Teleseismic P-Wave-Front Tracking*, Geophysical Journal International, Vol. 112, 39 – 66, 1993, 10.1111/j.1365-246X.1993.tb01435.x

Kolínský, P., Bokelmann, G., AlpArray Working Group, *Arrival Angles of Teleseismic Fundamental Mode Rayleigh Waves across the AlpArray*, Geophysical Journal International, Vol. 218, Issue 1, 115 – 144, 2019, 10.1093/gji/ggz081

Kolínský, P., Bokelmann, G., AlpArray Working Group, *Upper Mantle Imaging with AlpArray Surface Wave*

Diffraction: The Cameroon Volcanic Line, Geophysical Research Abstracts, Vol. 21, 2019

Krüger, F., Weber, M., *The Effect of Low-Velocity Sediments on the Mislocation Vectors of the GRF array*, Geophysical Journal International, Vol. 108, 387 – 393, 1992, 10.1111/j.1365-246X.1992.tb00866.x

Meltzer, A., Rudnick, R., Zeitler, P., Levander, A., Humphreys, G., Karlstrom, K., Ekström, G., Carlson, R., Dixon, T., Gurnis, M., Shearer, P., van der Hilst, R., *USArray Initiative*, GSA Today, 8 – 10, 1999

Molinari, I., Clinton, J., Kissling, E., Hetényi, G., Giardini, D., Stipčević, J., Dasović, I., Herak, M., Šipka, V., Wéber, Z., Gráczer, Z., Solarino, S., the Swiss-AlpArray Field Team, and the AlpArray Working Group, *Swiss-AlpArray Temporary Broadband Seismic Stations Deployment and Noise Characterization,* Advances in Geosciences., Vol. 43, 15 – 29, 2016, 10.5194/adgeo-43-15-2016

Muirhead, K. J., Datt, R., *The N-th Root Process Applied to Seismic Array Data*, Geophysical Journal International, Vol. 47 (1), 197 – 210, 1976

Müller, G, Kind, R., *Observed and Computed Seismogram Sections for the Whole Earth*, Geophysical Journal International, Vol. 44 (3), 699 – 716, 1976

Oliver, J., Murphy, L., WWNSS: *Seismology's Global Network of Observing Stations*, Science, Vol. 174 (4006): 254 – 261, 1971, 10.1126/science.174.4006.254

Pollitz, F., *Observations and Interpretation of fundamental Mode Rayleigh Wave-Fields Recorded by the Transportable Array (USArray)*, Journal of Geophysical Research, Vol. 113, 2008, 10.1029/2007JB005556

Rebeur-Paschwitz, E., *The Earthquake of Tokio 18. April 1889*, Nature, Vol. 40, 294 – 295, 1889, 10.1038/040294e0

Vignaroli, G, Faccenna, C., Jolivet, L., Piromallo, C., Rossetti, F., *Subduction Polarity Reversal at the Junction Between the Western Alps and the Northern Apennines, Italy*, Tectonophysics, Vol. 450, 34 – 50, 2008, 10.1016/j.tecto.2007.12.012

Vignaroli, G., Faccenna, C., Rossetti, F., Jolivet, L., *Insights from the Apennines Metamorphic Complexes and Their Bearing on the Kinematics Evolution of the Orogen*, Geological Society, London, Special Publications, Vol. 311, 235 – 256, 2009, 10.1144/SP311.9

Weber, M., *Subduction Zones: Their Influence on Traveltimes and Amplitudes of P-Waves*, Geophysical Journal International, Vol. 101, 529 – 544, 1990, 10.1111/j.1365-246X.1990.tb05568.x

Weber, M., *Traveltime and Amplitude Anomalies at the Seismic Broad-Band Array GRF*, Geophysical Journal International, Vol. 118, 57 – 74, 1994, 10.1111/j.1365-246X.1994.tb04675.x

Wielandt, E., *Propagation and Structural Interpretation of Non-Plane Waves*, Geophysical Journal International, Vol. 113, 45 – 53, 1993, 10.1111/j.1365-246X.1993.tb02527.x

Wysession, M. E., Shore, P. J., *Visualization of Whole Mantle Propagation of Seismic Shear Energy Using Normal Mode Summation*, Pure and Applied Geophysics, Vol .142 (2), 295 – 310, 1994

Networks

Albuquerque Seismological Laboratory (ASL)/USGS (1988): Global Seismograph Network (GSN - IRIS/USGS). International Federation of Digital Seismograph Networks. Dataset/Seismic Network. 10.7914/SN/IU

AlpArray Seismic Network. (2015). AlpArray Seismic Network (AASN) Temporary Component. AlpArray Working Group. 10.12686/ALPARRAY/Z3_2015

Aristotle University of Thessaloniki Seismological Network (1981): Permanent Regional Seismological Network operated by the Aristotle University of Thessaloniki. International Federation of Digital Seismograph Networks. Dataset/Seismic Network. 10.7914/SN/HT

Bogazici University Kandilli Observatory and Earthquake Research Institute (2001): Bogazici University Kandilli Observatory and Earthquake Research Institute. International Federation of Digital Seismograph Networks. Dataset/Seismic Network. 10.7914/SN/KO

CERN Seismic Network

Cesca, S., López Comino, J. Á., Kühn, D., Dahm, T. (2016). Array in Wittewierum, Netherlands. GFZ Data

https://doi.org/10.5194/se-2020-122
Preprint. Discussion started: 31 July 2020

Services. 10.14470/6P7561560569

Corinth Rift Laboratory Team And RESIF Datacenter. (2013). CL - Corinth Rift Laboratory Seismological Network (CRLNET). RESIF - Réseau Sismologique et géodésique Français. 10.15778/RESIF.CL

Croatian Seismograph Network

Danish Seismological Network

Department of Earth and Environmental Sciences, Geophysical Observatory, University of Munchen (2001): BayernNetz. International Federation of Digital Seismograph Networks. Dataset/Seismic Network. 10.7914/SN/BW

Deschamps, A., Beucler, E. (2013). POSA experiment. RESIF - Réseau Sismologique et géodésique Français. 10.15778/RESIF.ZH2016

Dr. Margarita Segou, Dr. John McCloskey, Dr. Brian Baptie, Dr. David Hawthorn (2016): Armatrice Sequence International. International Federation of Digital Seismograph Networks. Dataset/Seismic Network. 10.7914/SN/YR_2016

ESI SAS (Earth Science Institute of the Slovak Academy of Sciences). (2004). National Network of Seismic Stations of Slovakia. Deutsches GeoForschungsZentrum GFZ. 10.14470/FX099882

Estonian Seismic Network

Federal Institute for Geosciences and Natural Resources (BGR). (1976). German Regional Seismic Network (GRSN). Federal Institute for Geosciences and Natural Resources (BGR). 10.25928/MBX6-HR74

French Landslide Observatory – Seismological Datacenter / RESIF. (2006). Observatoire Multi-disciplinaire des Instabilités de Versants. Centre de données sismologiques / RESIF (Réseau Sismologique et géodésique Français). 10.15778/RESIF.MT

Friedrich Schiller University Jena and Thuringian Institute of Environment and Geology (2009): Thüringer Seismologisches Netz (TSN). International Federation of Digital Seismograph Networks. Dataset/Seismic Network. 10.7914/SN/TH

GEOFON Data Centre. (1993). GEOFON Seismic Network. Deutsches GeoForschungsZentrum GFZ. 10.14470/TR560404

Geological and Seismological Institute of Moldova (2007): Moldova Digital Seismic Network. International Federation of Digital Seismograph Networks. Dataset/Seismic Network. 10.7914/SN/MD

Geological Survey Department Cyprus (2013): Cyprus Broadband Seismological Network. International Federation of Digital Seismograph Networks. Dataset/Seismic Network. 10.7914/SN/CQ

Geological Survey-Provincia Autonoma di Trento (1981): Trentino Seismic Network. International Federation of Digital Seismograph Networks. Dataset/Seismic Network. 10.7914/SN/ST

Great Britain Seismograph Network

Guéguen, P., Coutant, O., Langlais, M. (2017). Maurienne Seismic Swarm 2017-2018. RESIF - Réseau Sismologique et géodésique Français. 10.15778/RESIF.YW2017

Heit, B., Weber, M., Tilmann, F., Haberland, C., Jia, Y., Carraro, C., Pesaresi, D. (2017). The Swath-D Seismic Network in Italy and Austria. GFZ Data Services. 10.14470/MF7562601148 Hessischer Erdbebendienst

INGV Experiments Network

INGV Seismological Data Centre. (2006, January 1). Rete Sismica Nazionale (RSN). Istituto Nazionale di Geofisica e Vulcanologia (INGV), Italy. 10.13127/SD/X0FXNH7QFY

INSN (1993): Irish National Seismic Network, operated by the Dublin Institute for Advanced Studies. International Federation of Digital Seismograph Networks. Dataset/Seismic Network. 10.7914/SN/EI

Institut Cartogràfic i Geològic de Catalunya (1984): Catalan Seismic Network. International Federation of Digital Seismograph Networks. Dataset/Seismic Network. 10.7914/SN/CA

Institut De Physique Du Globe De Paris (IPGP) & Ecole Et Observatoire Des Sciences De La Terre De Strasbourg (EOST). (1982). GEOSCOPE, French Global Network of broad band seismic stations. Institut de

https://doi.org/10.5194/se-2020-122
Preprint. Discussion started: 31 July 2020

Physique du Globe de Paris (IPGP). 10.18715/GEOSCOPE.G

Institute of Geophysics, Academy of Sciences of the Czech Republic (1973): Czech Regional Seismic Network. International Federation of Digital Seismograph Networks. Dataset/Seismic Network. 10.7914/SN/CZ

Institute of Geosciences, Energy, Water and Environment (2002): Albanian Seismological Network. International Federation of Digital Seismograph Networks. Dataset/Seismic Network. 10.7914/SN/AC

Institute of Seismology, U. O. H. (1980). The Finnish National Seismic Network. GFZ Data Services. 10.14470/UR044600

Instituto Geografico Nacional, Spain (1999): Spanish Digital Seismic Network. International Federation of Digital Seismograph Networks. Dataset/Seismic Network. 10.7914/SN/ES

International Miscellaneous Stations

ISNet - Irpinia Seismic Network

Jean-Philippe Malet, Mathilde Radiguet, Clément Hibert (2015): French Landslide Observatory – OMIV (Temporary data). International Federation of Digital Seismograph Networks. Dataset/Seismic Network. 10.15778/RESIF.MT

Kövesligethy Radó Seismological Observatory (Geodetic And Geophysical Institute, Research Centre for Astronomy and Earth Sciences, Hungarian Academy of Sciences (MTA CSFK GGI KRSZO)). (1992). Hungarian National Seismological Network. Deutsches GeoForschungsZentrum GFZ. 10.14470/UH028726

Laboratorio Subterraneo de Canfranc (2011): LSC (Laboratorio Subterraneo Canfranc). International Federation of Digital Seismograph Networks. Dataset/Seismic Network. 10.7914/SN/LC

Leipzig University (2001): SXNET Saxon Seismic Network. International Federation of Digital Seismograph Networks. Dataset/Seismic Network. 10.7914/SN/SX

MedNet Project Partner Institutions. (1990, January 1). Mediterranean Very Broadband Seismographic Network (MedNet). Istituto Nazionale di Geofisica e Vulcanologia (INGV), Italy. 10.13127/SD/FBBBTDTD6Q

National Institute for Earth Physics (NIEP Romania) (1994): Romanian Seismic Network. International Federation of Digital Seismograph Networks. Dataset/Seismic Network. 10.7914/SN/RO

National Institute of Geophysics, Geodesy and Geography - BAS (1980): National Seismic Network of Bulgaria. International Federation of Digital Seismograph Networks. Dataset/Seismic Network. 10.7914/SN/BS

National Observatory of Athens, Institute of Geodynamics, Athens (1997): National Observatory of Athens Seismic Network. International Federation of Digital Seismograph Networks. Dataset/Seismic Network. 10.7914/SN/HL

National Seismic Network of Turkey (DDA)

Norwegian National Seismic Network

Norwegian Seismic Array Network

OGS (Istituto Nazionale di Oceanografia e di Geofisica Sperimentale) (2016): North-East Italy Seismic Network. International Federation of Digital Seismograph Networks. Dataset/Seismic Network. 10.7914/SN/OX

OGS (Istituto Nazionale di Oceanografia e di Geofisica Sperimentale) and University of Trieste (2002): North-East Italy Broadband Network. International Federation of Digital Seismograph Networks. Dataset/Seismic Network. 10.7914/SN/NI

Polish Seismological Network

Portuguese National Seismic Network

Province Südtirol

RESIF. (1995). RESIF-RLBP French broadband network, RESIF-RAP strong motion network and other seismic stations in metropolitan France. RESIF - Réseau Sismologique et géodésique Français. 10.15778/RESIF.FR

RESIF. (2018). CEA/DASE broadband permanent network in metropolitan France. RESIF - Réseau Sismologique et géodésique Français. 10.15778/RESIF.RD

https://doi.org/10.5194/se-2020-122
Preprint. Discussion started: 31 July 2020

Royal Observatory of Belgium (1985): Belgian Seismic Network. International Federation of Digital Seismograph Networks. Dataset/Seismic Network. `10.7914/SN/BE`

San Fernando Royal Naval Observatory (ROA), Universidad Complutense De Madrid (UCM), Helmholtz-Zentrum Potsdam Deutsches GeoForschungsZentrum (GFZ), Universidade De Evora (UEVORA, Portugal), Institute Scientifique Of RABAT (ISRABAT, Morocco). (1996). The Western Mediterranean BB seismic Network. Deutsches GeoForschungsZentrum GFZ. `10.14470/JZ581150`

Scripps Institution of Oceanography (1986): IRIS/IDA Seismic Network. International Federation of Digital Seismograph Networks. Dataset/Seismic Network. `10.7914/SN/II`

Sector for Seismology, Institute of Hydrometeorology and Seismology of Montenegro (1982): Montenegrin Seismic Network. Dataset/Seismic Network. `10.7914/SN/ME`

Seismic Network of Tunisia

Serbian Seismological Network

Slovenian Environment Agency (2001): Seismic Network of the Republic of Slovenia. International Federation of Digital Seismograph Networks. Dataset/Seismic Network. `10.7914/SN/SL`

Swiss Seismological Service (SED) At ETH Zurich. (1983). National Seismic Networks of Switzerland. ETH Zürich. `10.12686/SED/NETWORKS/CH`

Technological Educational Institute of Crete (2006): Seismological Network of Crete. International Federation of Digital Seismograph Networks. Dataset/Seismic Network. `10.7914/SN/HC`

UK Schools Seismic Network

UK-Net, Blacknest Array

UniBAS

University of Athens (2008): University of Athens, Seismological Laboratory. International Federation of Digital Seismograph Networks. Dataset/Seismic Network. `10.7914/SN/HA`

University of Bari "Aldo Moro" (2013): OTRIONS, Seismic networks of Gargano Area (Italy). International Federation of Digital Seismograph Networks. Dataset/Seismic Network. `10.7914/SN/OT`

University of Genova (1967): Regional Seismic Network of North Western Italy. International Federation of Digital Seismograph Networks. Dataset/Seismic Network. `10.7914/SN/GU`

University of Lisbon Seismic Network

University of Patras, Geology Department, Seismological Laboratory (2000): PSLNET, permanent seismic network operated by the University of Patras, Greece. International Federation of Digital Seismograph Networks. Dataset/Seismic Network. `10.7914/SN/HP`

University of Trieste (1993): Friuli Venezia Giulia Accelerometric Network. International Federation of Digital Seismograph Networks. Dataset/Seismic Network. `10.7914/SN/RF`

Utrecht University (UU Netherlands) (1983): NARS. International Federation of Digital Seismograph Networks. Dataset/Seismic Network. `10.7914/SN/NR`

ZAMG - Zentralanstalt für Meterologie und Geodynamik (1987): Austrian Seismic Network. International Federation of Digital Seismograph Networks. Dataset/Seismic Network. `10.7914/SN/OE`

https://doi.org/10.5194/se-2020-122
Preprint. Discussion started: 31 July 2020

Solid Earth Discussions

Supplementary Materials

(1) Taiwan (C201802061550A)

https://www.dropbox.com/s/xgamskk6r6s39p1/Video.mp4?dl=0

(2) Southwest of Africa (C201801281603A)

https://www.dropbox.com/s/q37lk3y66jx50a5/Video.mp4?dl=0

(3) Central Italy (C201610300640A)

https://www.dropbox.com/s/50ucek6krftv502/Video.mp4?dl=0

(4) Southern Chile (C201612251422A)

https://www.dropbox.com/s/14h754xbh1us74u/Video.mp4?dl=0

(5) Eastern Russia (C201801250210A)

https://www.dropbox.com/s/tx3pesaaoqgixov/Video.mp4?dl=0

(6) Central Italy (C201608240136A)

https://www.dropbox.com/s/20jhg7iye4ugdkz/Video.mp4?dl=0

https://doi.org/10.5194/se-2020-122
Preprint. Discussion started: 31 July 2020

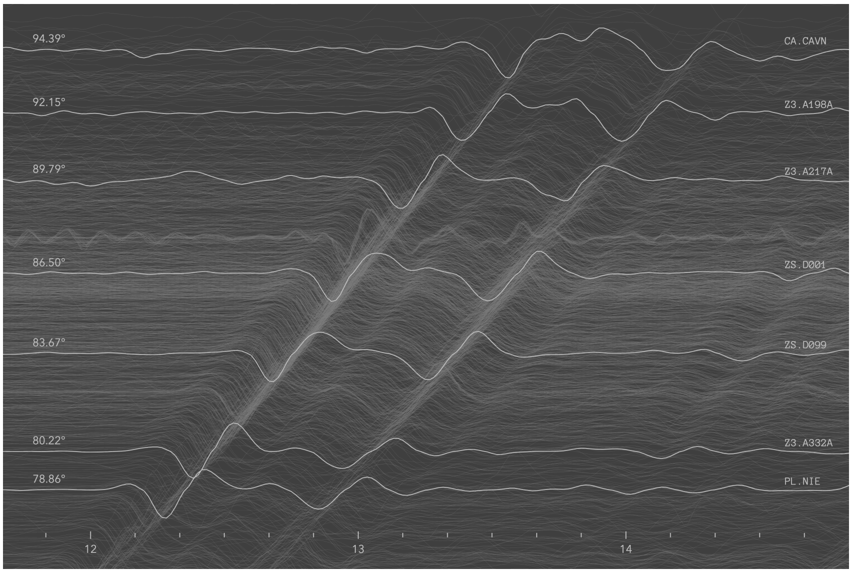

Fig. 16: Seismogram section of `P` arrivals for event No. 1, Taiwan (`C201802061550A`). Time axis is given in minutes after source time.

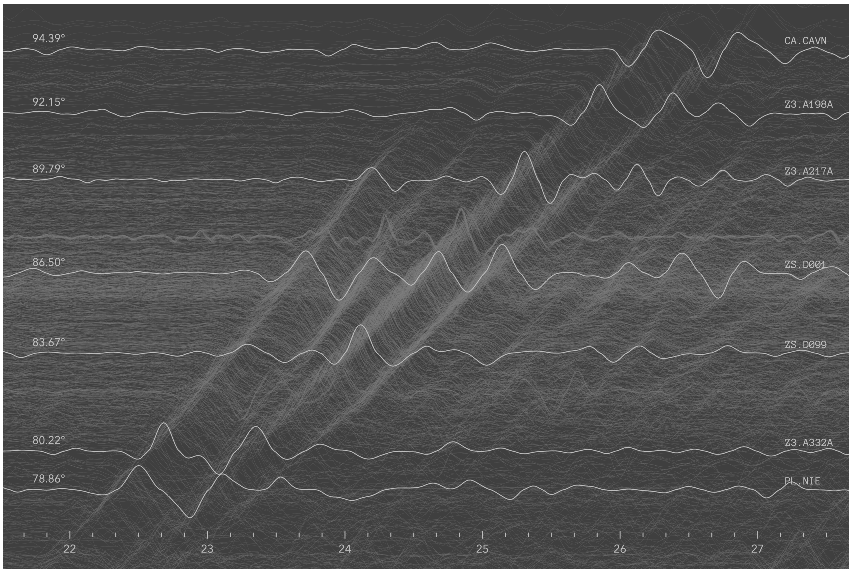

Fig. 17: Seismogram section of `S` arrivals for event No. 1, Taiwan (`C201802061550A`). Time axis is given in minutes after source time.

https://doi.org/10.5194/se-2020-122
Preprint. Discussion started: 31 July 2020

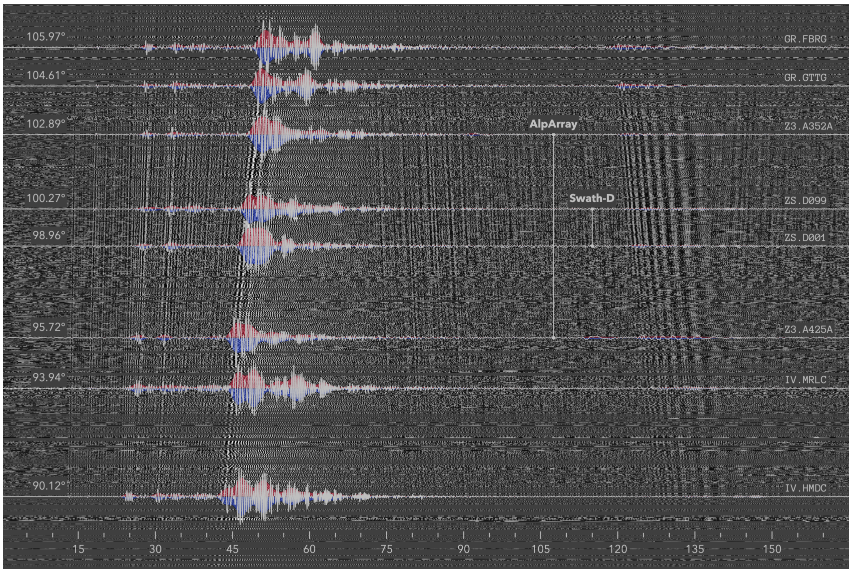

Fig. 18: Seismogram section for event No. 2, Southwest of Africa (`C201801281603A`). Time axis is given in minutes after source time.

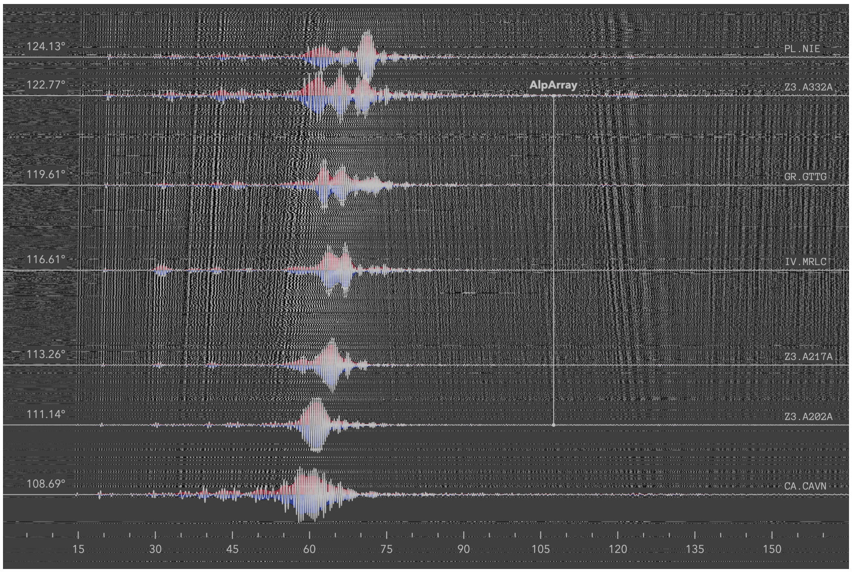

Fig. 19: Seismogram section for event No. 4, Southern Chile (`C201612251422A`). Time axis is given in minutes after source time.

https://doi.org/10.5194/se-2020-122
Preprint. Discussion started: 31 July 2020

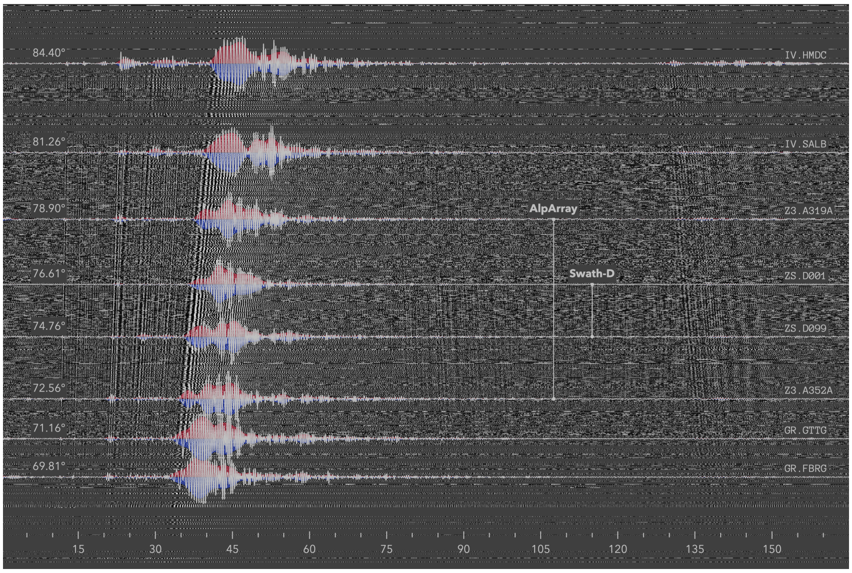

Fig. 20: Seismogram section for event No. 5, Eastern Russia (`C201801250210A`). Time axis is given in minutes after source time.

https://doi.org/10.5194/se-2020-122
Preprint. Discussion started: 31 July 2020

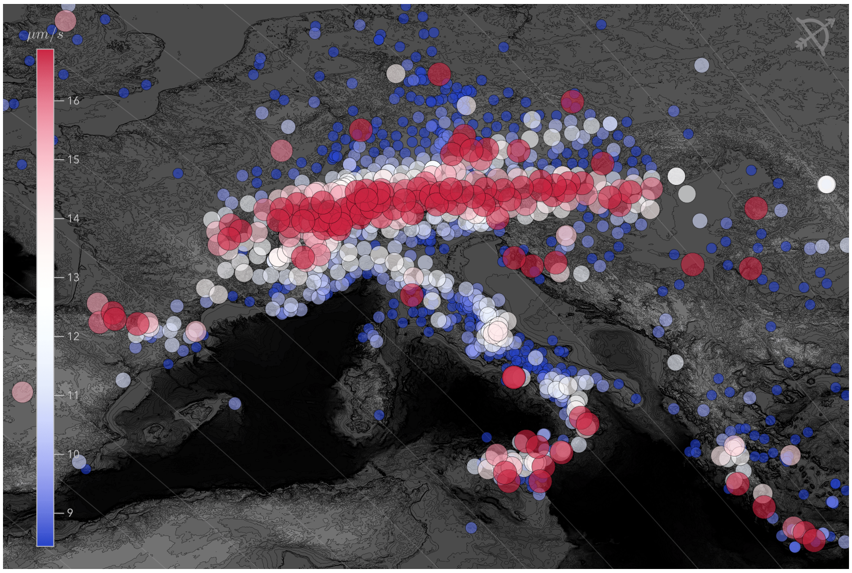

Fig. 21: Standard deviation of vertical ground velocity over a 2:45 *hour* period, starting at source time. Epicenter in Southern Chile, propagation direction southwest-to-northeast. Event No. 4, Southern Chile (`C201612251422A`).

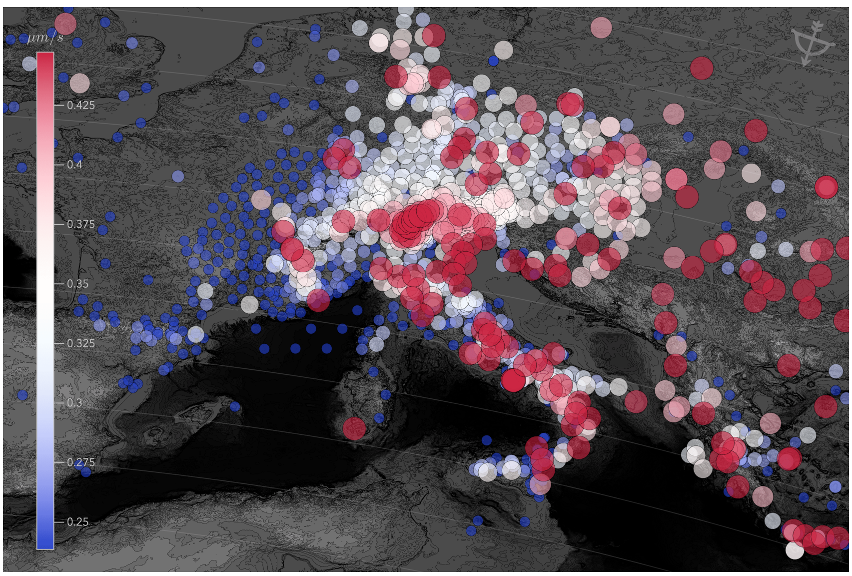

Fig. 22: Standard deviation of vertical ground velocity over a 2:45 *hour* period, starting at source time. Epicenter in Eastern Russia, propagation direction north-to-south. Event No. 5, Eastern Russia (`C201801250210A`).

https://doi.org/10.5194/se-2020-122
Preprint. Discussion started: 31 July 2020

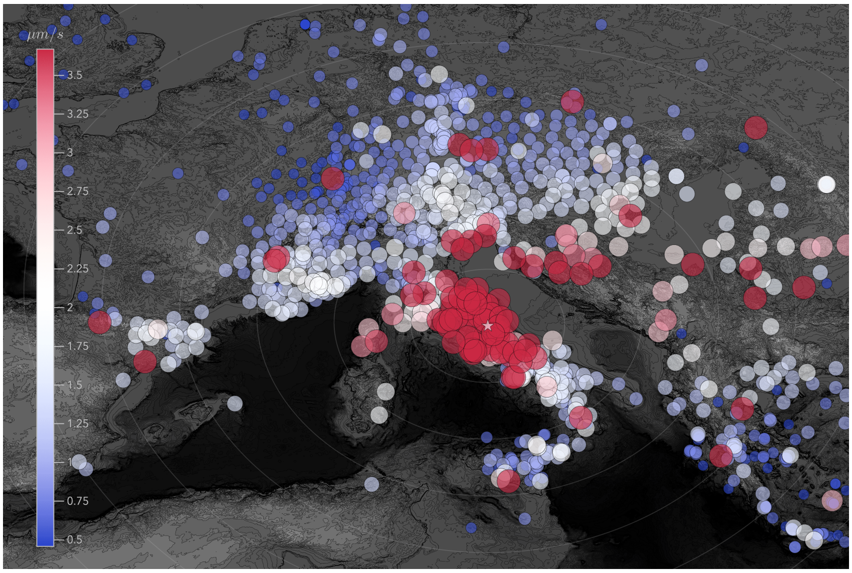

Fig. 23: Standard deviation of vertical ground velocity over a 3:40 *hour* period, starting at 10:00 *min* before source time. Epicenter in Central Italy marked with a white star, propagation direction outward. Event No. 6, Central Italy (`C201608240136A`).